INTERNATIONAL JOURNAL FOR NUMERICAL METHODS IN FLUIDS
Int. J. Numer. Meth. Fluids 0000; **00**:1–23 *Prepared using* fldauth.cls *[Version: 2002/09/18 v1.01]*

Residual based artificial viscosity for simulation of turbulent compressible flow using adaptive finite element methods

Murtazo Nazarov[a,*,†] and Johan Hoffman[b,‡]

[a] *Department of Mathematics, Texas A&M University 3368 TAMU, College Station, TX 77843, USA*
[b] *Computational Technology Laboratory, School of Computer Science and Communication, Royal Institute of Technology KTH, SE-10044 Stockholm, Sweden.*

SUMMARY

In this paper we present a finite element method with a residual based artificial viscosity for simulation of turbulent compressible flow, with adaptive mesh refinement based on a posteriori error estimation with sensitivity information from an associated dual problem. The artificial viscosity acts as a numerical stabilization, as shock-capturing, and as turbulence capturing for large eddy simulation (LES) of turbulent flow. The adaptive method resolves parts of the flow indicated by the a posteriori error estimates, but leaves shocks and turbulence under-resolved in a LES. The method is tested for examples in 2D and 3D, and is validated against experimental data. Copyright © 0000 John Wiley & Sons, Ltd.

KEY WORDS: compressible turbulent flow, large eddy simulation, adaptive finite element method, numerical stabilization, transonic flow, supersonic flow

1. Introduction

We consider the problem of computational simulation of turbulent compressible flow, where we seek a method that is numerically stable, computationally inexpensive and easy to implement, and which is general enough to allow for reliable simulation of flow in complex geometry, and over a range of Reynolds numbers and Mach numbers. We present an adaptive finite element method with residual based artificial viscosity, to model the effect of scales not resolved by the computational mesh, with the dual purpose of turbulence capturing and shock capturing. The mesh is adaptively refined according to a posteriori error estimates in the form of residuals weighted by the solution to an associated dual problem. The artificial viscosity is only active where the residual is large, corresponding to the solution being non-smooth, e.g. in shocks and turbulence. Stability of the finite element method is directly connected to the artificial

*Correspondence to: Murtazo Nazarov, Department of Mathematics, Texas A&M University 3368 TAMU, College Station, TX 77843, USA
†E-mail: murtazo@math.tamu.edu
‡E-mail: jhoffman@csc.kth.se

Received 8 June 2011
Revised 19 January 2012
Accepted 31 January 2012

viscosity, which constitutes the only numerical stabilization of the method. Since the artificial viscosity is proportional to the residual, minimal artificial viscosity is introduced in smooth parts of the flow. This work is an extension of [1], in which a similar method was proposed for unsteady compressible flow, but where an additional stabilization term was added in the form of a least squares stabilization of the convective part of the equations. A space-time finite element approximation was used, with continuous linear approximation in space and time, but since the test functions were constant in time a fully consistent least squares stabilization could not be constructed. Here we drop the least squares stabilization to improve accuracy in smooth parts of the flow, since the present stabilization is fully consistent, as it is based on the residuals of the equations.

Large eddy simulation (LES) can be interpreted as a form of turbulence capturing, where only the largest scales of the flow are resolved, while the small scales are modeled in a so called subgrid model. LES is based on a filter applied to the basic equations, which leads to new equations for the filtered variables together with subgrid terms that need to be modeled, see e.g. [2]. For compressible flow, the main focus for numerical methods has been to compute sharp and monotone approximations of shocks, see e.g. [3, 4, 5]. Methods for turbulent compressible flow either combine techniques separately developed for shock capturing and turbulence capturing, see e.g. [6, 7], or try to develop a unified approach, see e.g. [8]. Typical techniques introduce dissipation in the problem, modeling the effect of unresolved scales in the flow. Sources of artificial dissipation can thus be subgrid modeling, shock capturing or numerical dissipation (artificial viscosity, upwinding methods, stabilized finite element methods, etc.).

In [9, 10, 11] an approach to incompressible turbulent flow is developed, which we refer to as a General Galerkin (G2) method, where we let a residual based numerical stabilization in a finite element method play the role of a LES subgrid model, similar to a so called Implicit LES [2, 12]. Related work in the finite element community include LES based on variational multiscale methods [13, 14]. In our approach we avoid filtering of the equations and multiscale decomposition of the solution, but instead interpret the numerical approximations as weak solutions, where we adaptively refine the computational mesh with respect to an a posteriori estimate of the error in chosen output functionals, see e.g. [15, 16].

In this paper we extend our work to compressible turbulent flow, where a residual based artificial viscosity offers an unified approach to (i) numerical stabilization, (ii) turbulence and (iii) shock capturing. That a unified approach is possible should not come as a surprise, since artificial viscosities of various forms have been used for each of the three objectives (i)-(iii). In particular, the residual based artificial viscosity takes the same basic form as the classical Smagorinsky subgrid model [17], but with the rate of strain tensor replaced by the residual of the equations. The method we propose is closely related to the entropy viscosity approach as numerical stabilization [18, 19] (with a different choice of artificial viscosity), stabilized finite element methods such as SUPG and SD [5, 20, 21] (shock capturing without the advective stabilization), and hyperviscosity methods [22, 8, 23] (with a different artificial viscosity). Our motivation for choosing a residual based artificial viscosity is that it is a consistent stabilization, which is simple to implement for general finite element formulations, and which we find to be numerically stable for a range of Reynolds numbers and Mach numbers.

To test the functionality of the method we present numerical tests, for which experimental results are available, where we find that our method is numerically stable and that the numerical approximations closely match the experimental reference values, with very few degrees of freedom. We present a posteriori estimates of the error in output functionals of

the solution, which are used as error indicators for local mesh refinement.

The outline of the paper is the following: in Section 2 we introduce the basic equations, and in Section 3 we present the numerical method with the residual based artificial viscosity, and comment on its relation to other methods. In Section 4 we review a posteriori error estimation underlying the adaptive algorithm, and in Section 5 we present numerical results.

2. The basic equations

We consider fluid enclosed in a fixed (open) domain Ω in three-dimensional space $\mathbb{R}^3$ with boundary Γ over a time interval $I = [0, \hat{t}\,]$ with initial time zero and final time $\hat{t}$.

We seek the *density* ρ, *momentum* $\boldsymbol{m} = \rho\boldsymbol{u}$, with $\boldsymbol{u} = (\boldsymbol{u}_1, \boldsymbol{u}_2, \boldsymbol{u}_3)$ the *velocity*, and the *total energy* E as functions of $(\boldsymbol{x}, t) \in Q = \Omega \times I$, where $\boldsymbol{x} = (\boldsymbol{x}_1, \boldsymbol{x}_2, \boldsymbol{x}_3)$ denotes the coordinates in $\mathbb{R}^3$. The equations for $\hat{\boldsymbol{u}} \equiv (\rho, \boldsymbol{m}, E)$ read:

$$\begin{array}{rcll} \partial_t\rho + \nabla\cdot(\rho\boldsymbol{u}) &=& 0 & \text{in } Q,\\ \partial_t\boldsymbol{m} + \nabla\cdot(\boldsymbol{m}\otimes\boldsymbol{u} + p\mathbb{I}) &=& \boldsymbol{g} + \nabla\cdot(2\mu\varepsilon(\boldsymbol{u}) + \lambda(\nabla\cdot\boldsymbol{u})\mathbb{I}) & \text{in } Q,\\ \partial_t E + \nabla\cdot(E\boldsymbol{u} + p\boldsymbol{u}) &=& \nabla\cdot((2\mu\varepsilon(\boldsymbol{u}) + \lambda(\nabla\cdot\boldsymbol{u}))\cdot\boldsymbol{u} + \kappa\nabla T) & \text{in } Q,\\ \hat{\boldsymbol{u}}(\cdot, 0) &=& \hat{\boldsymbol{u}}^0 & \text{in } \Omega, \end{array} \tag{2.1}$$

where $p = p(\boldsymbol{x}, t)$ is the *pressure* of the fluid, $\otimes$ denotes the tensor product, $\mathbb{I}$ denotes the identity matrix in $\mathbb{R}^3$, $\partial_t = \partial/\partial_t$ and $\boldsymbol{g} = (\boldsymbol{g}_1, \boldsymbol{g}_2, \boldsymbol{g}_3)$ is a given *volume force* (like gravity) acting on the fluid, $\hat{\boldsymbol{u}}^0 = \hat{\boldsymbol{u}}^0(\boldsymbol{x})$ represents initial conditions, and

$$\varepsilon(\boldsymbol{u}) = \frac{1}{2}(\nabla\boldsymbol{u} + \nabla\boldsymbol{u}^T),$$

is the strain rate tensor and $\kappa \geq 0$ the thermal conduction parameter. The viscosity parameters are assumed to satisfy conditions $\mu > 0$, $\lambda + 2\mu > 0$. For simplicity in our approximation we choose $\lambda = 0$.

Further, the total energy $E = k + \theta$, where $k = \rho|\boldsymbol{u}|^2/2$ is the *kinetic energy*, with $|\boldsymbol{u}|^2 \equiv \boldsymbol{u}_1^2 + \boldsymbol{u}_2^2 + \boldsymbol{u}_3^2$, and $\theta = \rho T$ is the *internal energy* with T the *temperature* scaled so that $c_v = 1$, where c_v is the heat capacity under constant volume.

For high Reynolds numbers we may approximate the Navier-Stokes equations by inviscid flow, where the viscosity coefficients and thermal conductivity are zero, resulting in the Euler equation (2.1):

$$\begin{array}{rcll} \partial_t\rho + \nabla\cdot(\rho\boldsymbol{u}) &=& 0 & \text{in } Q,\\ \partial_t\boldsymbol{m} + \nabla\cdot(\boldsymbol{m}\otimes\boldsymbol{u} + p\mathbb{I}) &=& \boldsymbol{g} & \text{in } Q,\\ \partial_t E + \nabla\cdot(E\boldsymbol{u} + p\boldsymbol{u}) &=& 0 & \text{in } Q,\\ \hat{\boldsymbol{u}}(\cdot, 0) &=& \hat{\boldsymbol{u}}^0 & \text{in } \Omega. \end{array} \tag{2.2}$$

The number of unknowns including the pressure is six but there are only five equations in (2.1)-(2.2), and so we close the systems with the *state equation* of a *perfect gas*;

$$p = (\gamma - 1)\theta = (\gamma - 1)\rho T = (\gamma - 1)(E - \rho|\boldsymbol{u}|^2/2), \tag{2.3}$$

expressing the pressure p as a function of density ρ and temperature T, where $\gamma = c_p$ is the *adiabatic index* with c_p the heat capacity under constant pressure, and $(\gamma - 1)$ is the *gas constant*.

For a perfect gas, the *speed of sound* c is given by $c^2 = \gamma(\gamma - 1)T$, and the *Mach number* is defined as $M = |\boldsymbol{u}|/c$, with $\boldsymbol{u}$ the velocity of the gas.

3. Residual based artificial viscosity

Similar to shock capturing, we may use the term turbulence capturing, to mean computational methods without full resolution of all physical scales in the problem. Large eddy simulation (LES) is an example of turbulence capturing, where the flow is divided into resolved and unresolved scales by filtering the equations [2], or for finite element methods, by a decomposition of the approximation spaces into resolved and unresolved scales [13, 14]. A subgrid model is used to model the unresolved scales, typically by the introduction of dissipation. Either the subgrid model is constructed from physics arguments, or it is considered to be an effect of the numerical discretization, a so called Implicit LES [2]. In this paper we extend to compressible flow our work on incompressible turbulent flow, where we avoid filtering and scale decomposition, to instead interpret a finite element approximation as a weak solution with error control in functional output [9, 10, 11]. For a discussion on weak solutions as a model for high Reynolds number flow, see e.g. [9, 24, 25].

Residual based numerical stabilization of finite element methods for compressible flow was developed already in the 1980s [26, 27, 20], and has received continuous interest since then, see e.g. [28, 29]. The most well-known methods, such as SUPG, SD and GLS, take the form of a least squares stabilization together with shock capturing. The fact that the stabilization is based on the residual assures high accuracy in smooth parts of the flow. Various modifications of the basic methods have been developed, where the high order character of the stabilization is maintained. This includes multiscale approaches, where the stabilization is only active at the finest scales [30, 31, 14]. In relation to this family of methods, what we propose in this paper is simply to drop the least squares stabilization, and keep only the shock capturing terms. This approach is inspired by the work of Guermond and co-workers [18, 19], where a similar method is proposed, but with the artificial viscosity based on an entropy residual.

In the following sections we describe the finite element method we use in this paper, together with the residual based artificial viscosity, with the combined purpose of numerical stabilization, shock capturing and turbulence capturing.

Remark 3.1. The term of "shock-capturing" which is used in this paper is consistent with the definition of the shock-capturing term proposed by Johnson, Szepessy and Hansbo [32, 33, 34], it is not the same term used by Hughes and Mallet [35]. The discontinuity-capturing or shock-capturing terms proposed by Hughes and Mallet adds diffusion only in the crosswind direction of the flow close to discontinuities and shocks. However, according to our knowledge, there is no theoretical analyses explaining the robustness and convergence of the method available in the literature. Johnson and Szepessy modified this term such that it adds viscosity locally in all directions close to discontinuities. With this modification they were able to prove some important analytical results on the stabilized finite element methods. Dropping the streamline diffusion terms results in a method which is very similar to many artificial viscosity methods used in finite difference and finite volume communities. We have not tried to test the method

used by Hughes and Mallet with only a discontinuity capturing term, therefore we do not conclude that a similar approach works when only the shock-capturing in a crosswind direction is used.

3.1. Finite element approximation

Let $0 = t_0 < t_1 < ... < t_N = \hat{t}$, be a sequence of discrete time steps with associated time intervals $I_n = (t_{n-1}, t_n]$ of length $\Delta t_n = t_n - t_{n-1}$, and let $W_h \subset H^1(\Omega)$ be a finite element space consisting of continuous piecewise linear functions on a fixed mesh $\mathcal{T}_h = \{K\}$ of mesh size $h_K < 1$, with elements K. We first discretize the equations in space by a finite element method, and we then solve the resulting system in time with 3rd order explicit strong stability preserving Runge-Kutta methods.

The finite element spatial discretization of the compressible Euler equations (2.2) reads: for $n = 1, 2, \cdots, N$ find $\hat{\boldsymbol{u}}_h \equiv \boldsymbol{u}_h(t) \equiv (\rho_h(t), \boldsymbol{m}_h(t), E_h(t))$ with $\hat{\boldsymbol{u}}_h(t) \in \boldsymbol{X}_h \equiv W_h \times W_h^d \times W_h$, such that

$$(\partial_t \hat{\boldsymbol{u}}_h, \hat{\boldsymbol{v}}_h) + (\nabla \cdot \boldsymbol{f}(\hat{\boldsymbol{u}}_h), \boldsymbol{v}_h) + (\nabla \cdot \boldsymbol{f}_{visc}(\hat{\boldsymbol{u}}_h), \boldsymbol{v}_h) = 0, \tag{3.1}$$

for all test functions $\hat{\boldsymbol{v}}_h = (v_h^\rho, v_h^{\boldsymbol{m}}, v_h^E) \in \boldsymbol{X}_h$, where

$$(\boldsymbol{v}, \boldsymbol{w}) = \sum_{K \in \mathcal{T}_h} \int_K \boldsymbol{v} \cdot \boldsymbol{w} \, \mathrm{d}\boldsymbol{x}.$$

We denote by $\hat{\boldsymbol{u}}_n$ the solution at the discrete time steps t_n, that is $\hat{\boldsymbol{u}}_n \equiv \hat{\boldsymbol{u}}_h(t_n)$.

We define $\boldsymbol{u}_n$, p_n and T_n to be finite element functions in W_h^d, W_h and W_h, respectively, which are defined by their nodal values given by

$$\begin{aligned} \boldsymbol{u}_n(\boldsymbol{N}_i) &= \boldsymbol{m}_n(\boldsymbol{N}_i)/\rho_n(\boldsymbol{N}_i), \\ p_n(\boldsymbol{N}_i) &= (\gamma - 1)\rho_n(\boldsymbol{N}_i)T_n(\boldsymbol{N}_i), \\ T_n(\boldsymbol{N}_i) &= E_n(\boldsymbol{N}_i)/\rho_n(\boldsymbol{N}_i) - |\boldsymbol{u}_n(\boldsymbol{N}_i)|^2/2 \end{aligned} \tag{3.2}$$

for all nodes $\boldsymbol{N}_i$ in the mesh $\mathcal{T}_h$.

The fluxes at $t = t_n$ are defined as follows:

$$\boldsymbol{f}(\hat{\boldsymbol{u}}_h) = \begin{pmatrix} \rho \boldsymbol{u}_n \\ \boldsymbol{m}_n \otimes \boldsymbol{u}_n + p_n \mathbb{I} \\ (E + p)\boldsymbol{u}_n \end{pmatrix}, \quad \boldsymbol{f}_{visc}(\hat{\boldsymbol{u}}_h) = \begin{pmatrix} -\nu_n \nabla \rho_n \\ -\mu_n \varepsilon(\boldsymbol{u}_n) \\ -\mu_n \varepsilon(\boldsymbol{u}_n) \cdot \boldsymbol{u}_n - \kappa_n \nabla T_n \end{pmatrix}, \tag{3.3}$$

where the strain rate tensor is defined as above.

The dynamic artificial viscosity $\mu_n \equiv \mu_h(t_n)$ is computed as follows: Let Δt be a constant time-step and $\hat{\boldsymbol{u}}_n$, $\hat{\boldsymbol{u}}_{n-1}$, $\hat{\boldsymbol{u}}_{n-2}$ are solutions at times t_n, t_{n-1}, t_{n-2} respectively, and $\hat{\boldsymbol{u}}_n$ is continuous piecewise linear in space. Then, for each cell K we compute the residuals

$$\begin{aligned} R_\rho(\hat{\boldsymbol{u}}_n) =& \frac{1}{2\Delta t}(3\rho_n - 4\rho_{n-1} + \rho_{n-2}) + \nabla \cdot (\rho_n \boldsymbol{u}_n), \\ R_{\boldsymbol{m}}(\hat{\boldsymbol{u}}_n) =& \frac{1}{2\Delta t}(3\boldsymbol{m}_n - 4\boldsymbol{m}_{n-1} + \boldsymbol{m}_{n-2}) + \nabla \cdot (\boldsymbol{m}_n \otimes \boldsymbol{u}_n + p_n \mathbb{I}), \\ R_E(\hat{\boldsymbol{u}}_n) =& \frac{1}{2\Delta t}(3E_n - 4E_{n-1} + E_{n-2}) + \nabla \cdot (E_n \boldsymbol{u}_n + p_n \boldsymbol{u}_n). \end{aligned} \tag{3.4}$$

We then take the maximum of the absolute value of the residual in each cell to compute the following residual based artificial viscosity:

$$\mu_1|_K = C_1 h_K^2 \|\rho_n - \bar{\rho}_n\|_{\infty,\Omega} \max\left(\frac{\|R_\rho\|_{\infty,K}}{\|\rho_n - \bar{\rho}_n\|_{\infty,\Omega}}, \frac{\|R_{\boldsymbol{m}}\|_{\infty,K}}{\|\boldsymbol{m}_n - \bar{\boldsymbol{m}}_n\|_{\infty,\Omega}}, \frac{\|R_E\|_{\infty,K}}{\|E_n - \bar{E}_n\|_{\infty,\Omega}} \right), \tag{3.5}$$

where $\|\rho_n - \bar{\rho}_n\|_{\infty,\Omega}, \|\boldsymbol{m}_n - \bar{\boldsymbol{m}}_n\|_{\infty,\Omega}, \|E_n - \bar{E}_n\|_{\infty,\Omega}$ are normalization terms, with $\bar{\rho}_n, \bar{\boldsymbol{m}}_n, \bar{E}$ denoting a space averaged values over Ω of the density, momentum and energy.

As in [18, 19] we compute the maximum artificial viscosity, $\mu_{\max}$ as

$$\mu_{\max}|_K = C_2 h_K \|\rho_n\|_{\infty,K} \| |\boldsymbol{u}_n| + \sqrt{\gamma T_n} \|_{\infty,K}, \tag{3.6}$$

and

$$\mu_n|_K = \min(\mu_{\max}|_K, \mu_1|_K), \quad \kappa_n|_K = \frac{\mathcal{P}}{\gamma - 1}\mu_n|_K, \quad \nu_n|_K = \frac{\mathcal{P}}{\|\rho_n\|_{\infty,K}}\mu_n|_K, \tag{3.7}$$

where $\mathcal{P} \approx 0.1$ is an artificial Prandtl number, $C_1 = 1$ typically and from simple 1D analyses it is easy to show that $C_2 = 0.5$.

3.2. Time-stepping

The time-stepping is done by explicit 3rd order Runge-Kutta methods. The r stage explicit Runge-Kutta method for (3.1) is defined as follows:

$$\hat{\boldsymbol{u}}_{n+1} = \hat{\boldsymbol{u}}_n + \Delta t_n (b_1 \boldsymbol{k}_1 + b_2 \boldsymbol{k}_2 + \cdots + b_r \boldsymbol{k}_r), \tag{3.8}$$

where the coefficients b_i are obtained from the Butcher tableau and $\boldsymbol{k}_i$ is recursively computed by solving a mass matrix linear system at each step.

The mass matrix is symmetric positive definite and is assembled once, while the right hand side vector for computing $\boldsymbol{k}_i$ is assembled at every stage. There are a number of iterative solvers that can solve the system fast.

For a given CFL number the timestep is computed by

$$\Delta t_n = \text{CFL} \min_{K \in \mathcal{T}_h} (h_K / (|\boldsymbol{u}_n| + c))_K,$$

where h_K is the cell diameter for element K in the mesh $\mathcal{T}_h$ and the CFL number in the numerical examples of this paper is typically chosen as 0.4.

3.3. Boundary conditions

In this paper we consider wind tunnel problems in two and three space dimensions. The inflow and outflow boundary conditions are imposed according to characteristic variables on the boundary nodes, see for example Löhner [36]. For the supersonic case, for instance, all variables are imposed at inflow, while nothing is set at outflow.

We use a slip condition at the wall boundaries, where the normal velocity is set to be zero at the boundary. This condition is also referred to as a reflecting boundary condition.

The details of the implementation of the different boundary conditions are given in [37].

4. Adaptive method

A posteriori error estimation underlies our adaptive algorithm, in the form of a bound on the error in a functional of the solution. For a turbulent solution, pointwise convergence of an approximate solution to an exact solution cannot be expected, but mean value functionals of the solution can still be well-posed, see e.g. [38].

4.1. A posteriori error estimation

To estimate the error in a target functional $\mathcal{M}(\hat{\boldsymbol{u}})$, we introduce the following dual problem: Find $\Phi = (\phi_\rho, \phi_{\boldsymbol{m}}, \phi_E)$ such that

$$\begin{aligned} -\partial_t \Phi - \boldsymbol{f}'(\hat{\boldsymbol{u}}_h)^T \nabla \Phi &= \Psi_Q \qquad \text{in } Q, \\ (\boldsymbol{n} \cdot \boldsymbol{f}'(\hat{\boldsymbol{u}}_h))^T \Phi &= \Psi_\Gamma \qquad \text{on } \Gamma \times I, \\ \Phi(\cdot, \hat{t}) &= 0 \qquad \text{in } \Omega, \end{aligned} \tag{4.1}$$

where ϕ_ρ is *dual density*, $\phi_{\boldsymbol{m}}$ *dual momentum* and ϕ_E *dual energy*, $\boldsymbol{f}'(\hat{\boldsymbol{u}}_h)^T$ is the transpose of the Jacobian matrix $\boldsymbol{f}'(\hat{\boldsymbol{u}}_h)$, and $\Psi \equiv \{\Psi_Q, \Psi_\Gamma\}$ with $\Psi_Q \in L_2\left(I; L_2(\Omega) \times [L_2(\Omega)]^d \times L_2(\Omega)\right)$ and $\Psi_\Gamma \in L_2\left(I; L_2(\Gamma) \times [L_2(\Gamma)]^d \times L_2(\Gamma)\right)$ are source terms, which define a target functional by

$$\mathcal{M}(\hat{\boldsymbol{u}}) = \int_Q \hat{\boldsymbol{u}} \cdot \Psi_Q \,\mathrm{d}x \,\mathrm{d}t + \int_I \int_\Gamma \hat{\boldsymbol{u}} \cdot \Psi_\Gamma \,\mathrm{d}S \,\mathrm{d}t. \tag{4.2}$$

The expression $\boldsymbol{n} \cdot \boldsymbol{f}'(\hat{\boldsymbol{u}}_h)$ is referred to as the normal flux Jacobian, where $\boldsymbol{n}$ is an outward unit normal to Γ. Boundary conditions for the dual problem depend on the target functional and boundary conditions of the corresponding primal equation.

Since we cannot solve the continuous problem (4.1) analytically, we replace Φ by a finite element approximation Φ_h. We use a similar finite element method to compute Φ_h, as we use for the primal problem. With standard techniques, we can derive the following a posteriori error estimate [39, 1, 40, 10]:

$$\begin{aligned} |\mathcal{M}(\hat{\boldsymbol{u}}) - \mathcal{M}(\hat{\boldsymbol{u}}_h)| &\leq \sum_n \sum_{K \in \mathcal{T}_n} \int_{I_n} C_h h_K |R(\hat{\boldsymbol{u}}_h)|_K \cdot |D\Phi|_K \\ &\quad + \sum_n \sum_{K \in \mathcal{T}_n} \int_{I_n} |Vis(\hat{\boldsymbol{u}}_h; \pi_h \Phi)_K| \,\mathrm{d}t + h.o.t. \\ &\equiv \sum_{n,K} \mathcal{E}_n^K + h.o.t., \end{aligned} \tag{4.3}$$

where $\mathcal{M}(\hat{\boldsymbol{u}})$ is a target functional, $R(\hat{\boldsymbol{u}}_h) = (R_\rho(\hat{\boldsymbol{u}}_h), R_{\boldsymbol{m}}(\hat{\boldsymbol{u}}_h), R_E(\hat{\boldsymbol{u}}_h))$ is the residual of the Euler equations (2.2), $D\Phi$ denotes a space-time derivative of Φ, $C_h = 1/2$ is an interpolation constant and *h.o.t.* denotes higher order terms from the linearization of the system. The term

$$Vis(\hat{\boldsymbol{u}}_h; \pi_h \Phi) := (\nabla \cdot \boldsymbol{f}_{visc}(\hat{\boldsymbol{u}}_h), \pi_h \Phi)$$

denotes a contribution from the residual based artificial viscosity in the finite element discretization.

4.2. Computation of the drag coefficient

We compute the drag coefficient of a body as:

$$C_{pd} = \frac{F_{pd}}{1/2\rho_\infty |\boldsymbol{u}_\infty|^2 A}, \tag{4.4}$$

where $F_{pd} = \frac{1}{|I|}\int_I \int_{\Gamma_{body}} p(\boldsymbol{n}\cdot\boldsymbol{e}_{pd})\,\mathrm{d}S\,\mathrm{d}t$ is the drag force, $\boldsymbol{e}_{pd} = (1,0,0)^T$ is a unit vector in the flow direction, Γ_{body} is a surface of the body, ρ_∞ is the free stream density and $\boldsymbol{u}_\infty$ is the free stream velocity of the fluid, and A is a reference area. In this paper we approximate high Reynolds number flows by the Euler equations together with residual based artificial viscosity. The pressure drag has most contribution to the total drag force for the bluff body problems we consider here, and thus shear stress is neglected.

The dual problem is stabilized in the same way as the primal problem in Section 3 and is solved backward in time. We choose the drag coefficient of a body as target functional, so that $\mathcal{M}(\hat{\boldsymbol{u}}) = \frac{1}{|I|}\int_I \int_{\Gamma_{body}} p\boldsymbol{n}\cdot\boldsymbol{e}_{pd}\,\mathrm{d}S\,\mathrm{d}t$. This corresponds to that $\Psi_Q = 0$, and we have the following boundary condition for the dual problem (4.1):

$$\begin{aligned} \phi_{\boldsymbol{m}}\cdot\boldsymbol{n} &= \frac{1}{|I|}\boldsymbol{e}_{dp} \quad && \text{on } \Gamma_{body}\times I, \\ \phi_{\boldsymbol{m}}\cdot\boldsymbol{n} &= 0 && \text{on } \Gamma_{wall}\setminus\Gamma_{body}\times I, \\ \Phi &= 0 && \text{on } \Gamma_{outflow}\times I. \end{aligned} \tag{4.5}$$

We formulate the following adaptive algorithm:

Algorithm 1. *Given a tolerance TOL, start from an initial coarse mesh $\mathcal{T}_h^0$, with $k = 0$:*

1 *Compute an approximation to the primal solution on $\mathcal{T}_h^k$;*
2 *Compute an approximation of the dual solution on the same mesh;*
3 *Compute the error indicator defined in* (4.3)*, if $\sum_{n,K}\mathcal{E}_n^K < $ TOL, then STOP;*
4 *Refine a fixed fraction of cells in $\mathcal{T}_h^k$ with largest error indicators to get a new mesh $\mathcal{T}_h^{k+1}$;*
5 *Set $k = k+1$ and go to 1.*

Further, the estimate of the error in the drag coefficient $\bar{\mathcal{E}}_{dp}$ is obtained by normalization of the total error:

$$\bar{\mathcal{E}}_{dp} = \frac{\sum_{n,K}\mathcal{E}_n^K}{1/2\rho_\infty|\boldsymbol{u}_\infty|^2 A}, \tag{4.6}$$

and we define a stability factor as

$$\mathcal{S} = \int_I \sum_K |D\Phi|_K\,\mathrm{d}t. \tag{4.7}$$

Remark 4.1. According to our previous experience an error bound of the type (4.3) appears to be a good indicator for adaptive mesh refinement, see e.g. [1, 16, 11]. However, since (4.3) is overestimating the true target error $\mathcal{M}(\hat{\boldsymbol{u}}) - \mathcal{M}(\hat{\boldsymbol{u}}_h)$, there is no theoretical evidence available at this moment to show convergence of Algorithm 1. In our computational results shown in this paper we observe that, though the target functional converges to its reference values the error bound (4.3) may not always get smaller with mesh refinement. We leave a detailed analysis of this issue for the future research.

5. Numerical results

To test our method we perform numerical experiments, in the form of external flow past a body in a wind tunnel. In particular, we consider flow around a circular cylinder and a sphere. The flow is complex, with compressibility effects such as shocks, contact discontinuities and rarefaction waves, separation and turbulent wakes, see e.g. [41, 42, 43].

In the simulations we use dimensionless variables. If L is a characteristic length, then we normalize the density ρ^*, the speed of sound c^* and the temperature T^*, by their free stream values ρ_∞, c_∞ and T_∞ as the following: $\rho = \frac{\rho^*}{\rho_\infty}$, $c = \frac{c^*}{c_\infty}$, $T = \frac{T^*}{T_\infty}$, $p = \frac{p^*}{\rho_\infty c_\infty^2}$, $u = \frac{u^*}{c_\infty}$, $M_\infty = \frac{u^*}{c_\infty}$, $\boldsymbol{x} = \frac{\boldsymbol{x}^*}{L}$, and we use non-dimensional time $t = \frac{t^* c_\infty}{L}$.

Accurate computation of aerodynamic forces, such as drag and lift, is not trivial. For high Mach numbers and Reynolds numbers, wave drag due to shocks is the main contribution to drag force [44], and therefore the inviscid Euler equations are a reasonable approximation for the transonic and supersonic flows we consider in this paper.

First we study two problems in two space dimensions where numerical reference results are available: supersonic flow in a wind tunnel with forward-facing step, and flow past a circular cylinder. The purpose of these test problems is to illustrate some basic features of the method. We show that the residual based artificial viscosity presented in this paper gives accurate results by adding small amounts of viscosity only in regions with sharp discontinuities, and the wake. The adaptive algorithm is not used in these test cases, instead the computations are done for given fixed meshes. We show that the artificial viscosity is localized for the fine mesh, however the basic compressible flow features for the problems are still captured well for the coarse mesh.

We then continue with benchmark problems in three space dimensions including turbulent, where experimental data is available.

5.1. Mach 3 flow in a wing tunnel with a step

We consider Mach 3 flow in a wind tunnel with a step. This is a well known benchmark used for testing new methods since [3].

The wind tunnel with length 3 and height 1 contains a step with height 0.2, situated at a distance 0.6 from the inflow. The initial data for the problem is $\rho = 1.4, \boldsymbol{m} = (4.2, 0), e = 8.8$. The inflow boundary condition has the same values as the initial state, a slip boundary condition is applied on the walls of the channel. We are in the supersonic regime, so all characteristics of the Euler equations go out of the outflow boundary, therefore no physical boundary conditions are needed at the outflow. To avoid an unphysical numerical boundary layer created from the singular point of the step we round off the corner with a relatively small fixed curvature. This approach removes any numerical errors from the singularity, and there is no need to apply any special treatment of the boundary condition as it is suggested by Woodward and Collela in [3]. Usually, for numerical tests this simulation is done until time $t = 4$.

We use three different meshes: a coarse mesh with 6 939 nodes, 13 512 cells and $h = 0.025$; a medium with 27 389 nodes, 54 048 cells and $h = 0.0125$; and a fine mesh with 153 864 nodes, 306 156 cells and $h = 0.00763$. We present our results in Figure 1. We plot 30 contours of the density and the magnitude of the residual based artificial viscosity from the coarse, medium and fine meshes. We observe that even for the coarsest mesh the method captures the

right locations of the strong shock and a contact discontinuity is clearly visible. The contact discontinuity is resolved well in the finest mesh. The medium mesh corresponds approximately to the same mesh of size 80×240 which is used in [3]. The approximation obtained by the residual based viscosity used in this paper is comparable with the high order finite difference schemes used in [3].

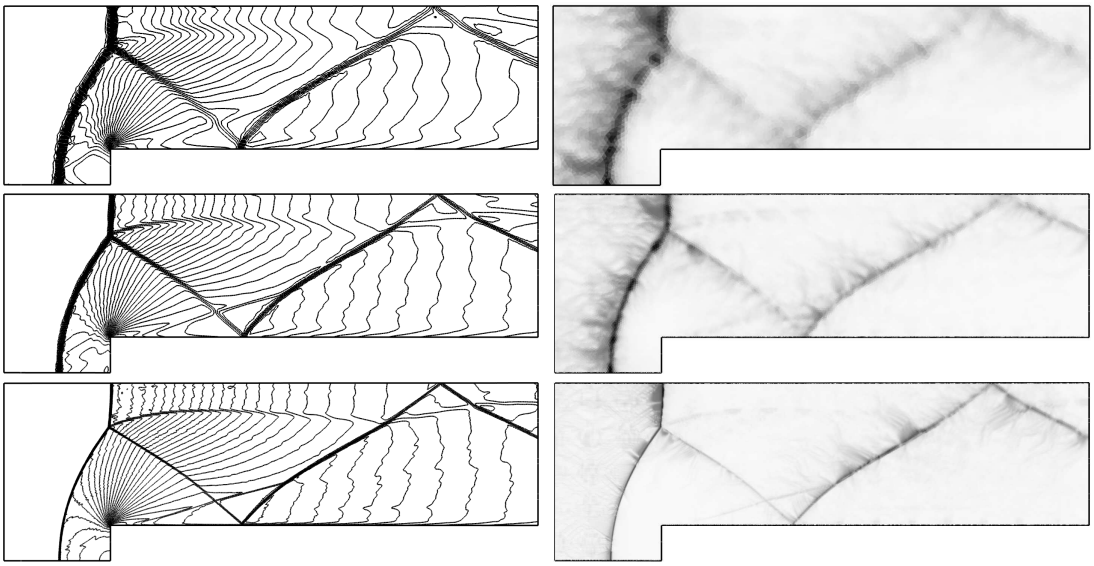

Figure 1. Wind-tunnel with forward-facing step: Colormap and 30 contours of density for the coarsest mesh, $h = 0.025$, $0.1775 \leq \rho \leq 6.0906$, $1.0e-4 \leq \mu \leq 0.0657$, at the top, medium mesh, $h = 0.0125$, $0.1245 \leq \rho \leq 6.2552$, $2.45e-5 \leq \mu \leq 0.0373$, at the middle, and finest mesh, $h = 0.00763$, $0.1245 \leq \rho \leq 6.2552$, $6.58e-6 \leq \mu \leq 0.0128$, at the bottom.

5.2. Supersonic flow around a 2D circular cylinder

Consider a wind tunnel of size $[0, 3] \times [0, 2]$ with a circular cylinder of radius 0.2 located at $(0.8, 1)$. Inviscid supersonic flow with $M = 2.52$ enters the tunnel. The simulation is done for two meshes: a coarse mesh of 5 992 nodes and 11 680 cells with mesh size $h_K \approx 0.0395$; and a fine mesh of 94 048 nodes and 186 880 cells with mesh-size $h_K \approx 0.00923$.

We present results from the computation in Figure 2, where solutions from the coarse and fine meshes are presented, at times $t = 0.6$ and $t = 15$. A detached strong bow shock develops in front of the cylinder and gets reflected at the wall boundaries, creating a Mach stem, at which a Rayleigh instability appears from the point of triple shocks. The Rayleigh instability is difficult to capture, and high accuracy is needed in the numerical approximations [3]. We see that even for the coarse mesh the instability pattern is here visible, and becomes more clear for the fine mesh. At the earlier time the solution appears stable and symmetric, after which the wake starts to oscillate, which is captured by the fine mesh.

The residual based artificial viscosity is plotted in the right column of Figure 2, where we use a grayscale to show the magnitude of the artificial viscosity, which is found to be highly

localized and becomes even sharper as the mesh is refined.

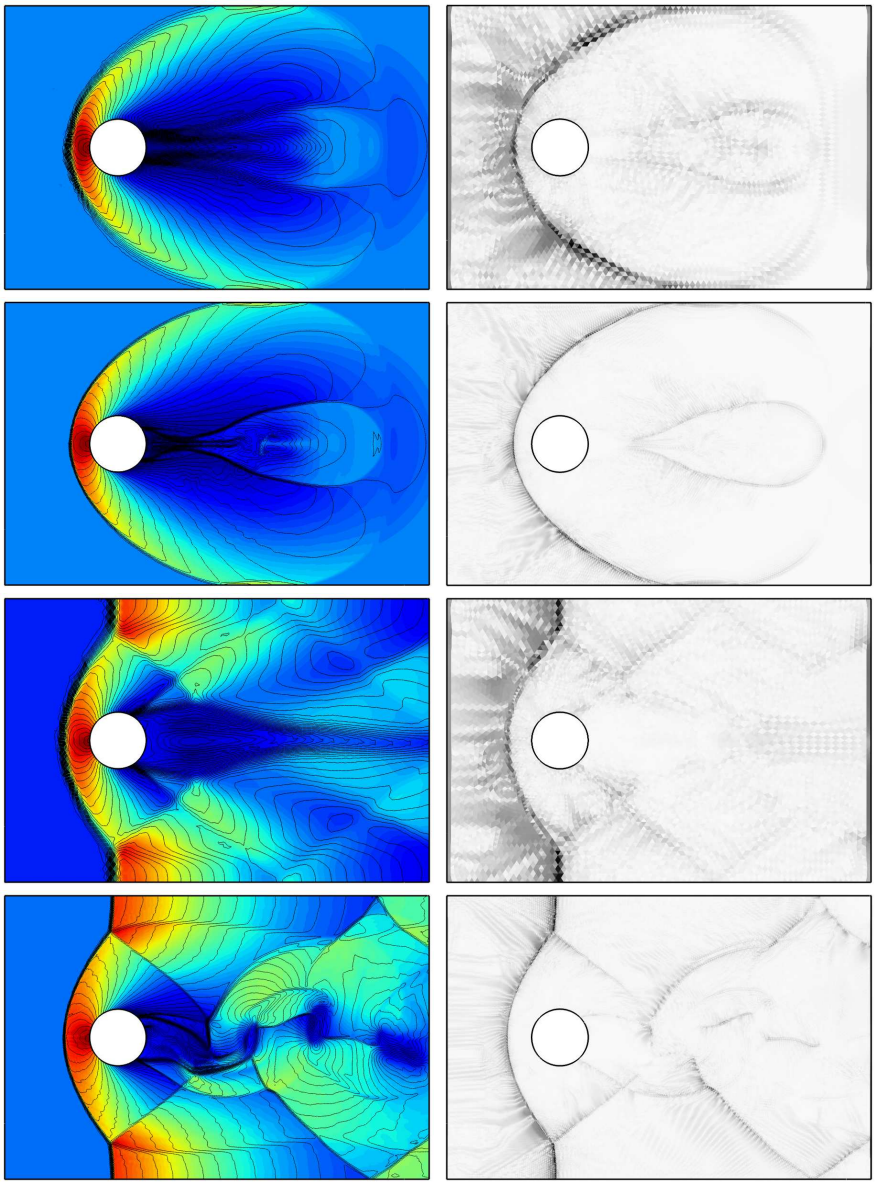

Figure 2. 2D supersonic flow: The color-map of the density and 30 isosurfaces of the Mach number are plotted in the left column. The artificial viscosity is plotted at the right column. The first row: coarse mesh $t = 0.6$, $0.12 \leq \rho \leq 5.04$, $7.45e-8 \leq \mu_n \leq 0.0954$ and $0.0135 \leq M \leq 3,17$; second row: fine mesh $t = 0.6$, $0.036 \leq \rho \leq 5.28$, $3.64e-11 \leq \mu_n \leq 0.0235$ and $0.0031 \leq M \leq 4.078$; third row: coarse mesh $t = 15$, $0.66 \leq \rho \leq 5.23$, $8.74e-5 \leq \mu_n \leq 0.120$ and $0.0141 \leq M \leq 2.58$; fourth row: fine mesh $t = 15$, $0.157 \leq \rho \leq 5.354$, $2.86e-06 \leq \mu_n \leq 0.0296$ and $0.0126 \leq M \leq 3.463$.

5.3. 3D compressible flow around a sphere

In this section we consider a wind tunnel in 3D with a sphere inside. The dimension of the tunnel is $[-3,3]\times[-0.5,0.5]\times[-0.5,0.5]$, with a sphere of radius 0.037 located at the center of origin. The initial mesh has 10 220 nodes and 55 492 tetrahedrons. We perform the adaptive Algorithm 1 for different Mach numbers to compute the drag force as the target functional.

For this problem there are experimental data available for different Mach and Reynolds numbers, see e.g. [45, 46, 47]. In our computations we consider three Mach numbers: a transonic case $M_\infty = 0.98$; and supersonic cases $M_\infty = 1.4, 3$. The corresponding reference values for drag is ~ 0.84, ~ 1 and ~ 0.9, respectively [45, 46, 47]. The experimental analysis from the given references show that the drag coefficient increases rapidly in the transonic regime, and continues to increase up to $M \sim 1.65$. Then, the value slowly decreases for further increase of the Mach number.

Figure 3 shows drag coefficients from different adaptive iterations and Mach numbers. We plot the corresponding experimental values with dashed lines. Figure 4 shows some more computational results of the adaptive algorithm. The top-left figure presents the change of the total error indicators $\bar{\mathcal{E}}_{dp}$ as a function of number of vertices. As we have mentioned earlier, though this error indicator is good criterion for the mesh refinement, it is overestimating the true error of the functional of interest. Since, the estimate (4.3) involves only absolute values, we loose the advantage of cancellation in the integral of the error estimate and the approximate solution of the dual problem also influence the accuracy of (4.3). The plot on the top-right shows the value of the stability factor defined in (4.7). We then plot the mean value in time of the drag coefficient for different adaptive iterations and Mach numbers in the lower-left plot of Figure 4, and a quality indicator C_{dp}/C_{dref} in the lower-right plot. We note that the quality of time averages for the case $M = 0.98$ would improve if we would use a longer time integral, but that was computationally too expensive in this study.

The experimental data which we used in this paper have approximately 5 to 10% relative errors. Therefore, the adaptive algorithm and the residual based viscosity gives good results for the drag coefficient, with respect to the experimental data.

Figure 5 shows the computational approximations of the primal and dual solutions. In the left column we plot the contours of the Mach numbers together with the velocity streamlines, and in the right column we plot the contours of the first component of the dual momentum $\phi_{\boldsymbol{m}_1}$ together with the sonic line. The results are shown only for the finest meshes. For all cases the separation of the flow starts from the attached shock waves. As the Mach number increases the position of the attached shock moves towards the back of the sphere. Therefore, the recirculation region behind the sphere shrinks. We see from the figures that the flow behaves more steadily and has a symmetric flow pattern for higher Mach numbers. Moreover, the dual solution is large in the wake for the transonic case, while it is not for the supersonic case; it shows that the wake needs to be resolved accurately for lower Mach numbers, whereas the upstream and the central parts of the bow shock is most important for the supersonic regime.

We plot the initial mesh with 10 220 vertices and 55 492 tetrahedrons in the first row of Figure 6. After each iteration of the adaptive algorithm 5% of the cells with the highest error contribution are marked for the refinement. The second row is the mesh which is obtained after nine adaptive iterations for $M_\infty = 0.98$, with 57 442 vertices and 308 600 cells. The third and fourth rows describe the final mesh for $M_\infty = 1.4$, with 61 097 vertices and 329 604 cells, and $M_\infty = 3$, with 57 442 vertices and 308 600 cells, respectively. The left column of

Figure 6 is the xz-plane at $y = 0$ and the right column is a zoomed view of the sphere and the yz-plane at $x = 0.037$ just behind the sphere. In order to reduce the geometry error in the approximation of the sphere surface, we project the new vertices of the refinement to the exact boundary surface. For all Mach numbers the area close to the attached shock wave to the sphere is finest resolved. The upstream flow has more effects on the drag coefficient than the downstream flow.

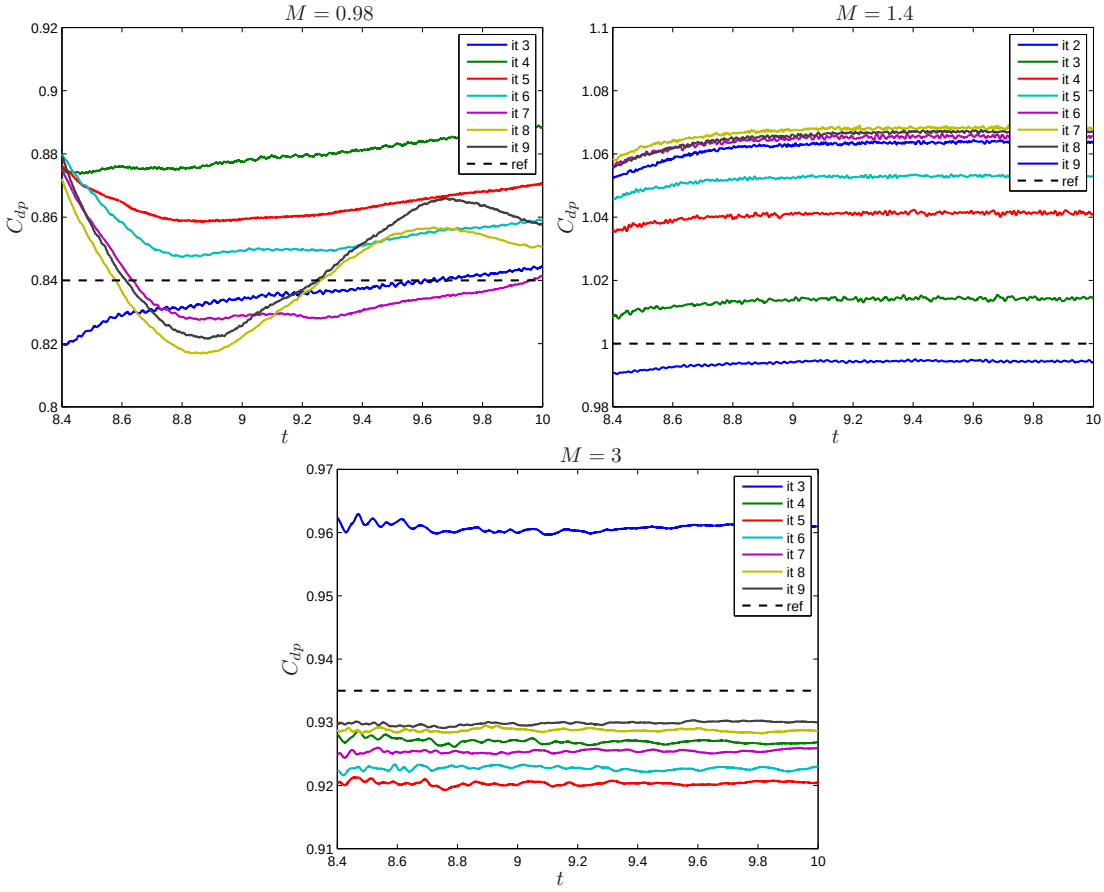

Figure 3. Sphere: The drag coefficient C_{dp} versus time for different Mach numbers and adaptive iterations.

5.4. 3D compressible flow around a circular cylinder

We next consider flow past a 3D circular cylinder. A cylinder of diameter 0.0254 is located at the origin of the channel of dimension $-2 \leq x \leq 2$, $-0.305 \leq y \leq 0.305$ and $0 \leq z \leq 0.12$. The initial mesh consists of 9 034 nodes and 43 323 tetrahedrons.

Experimental data is available by Murthy & Rose [42, 48] for different Mach numbers, at high Reynolds numbers. According to the experimental data, there is a rapid increase in the drag coefficient when M_∞ increases toward 1, while it decreases slowly for further increase of

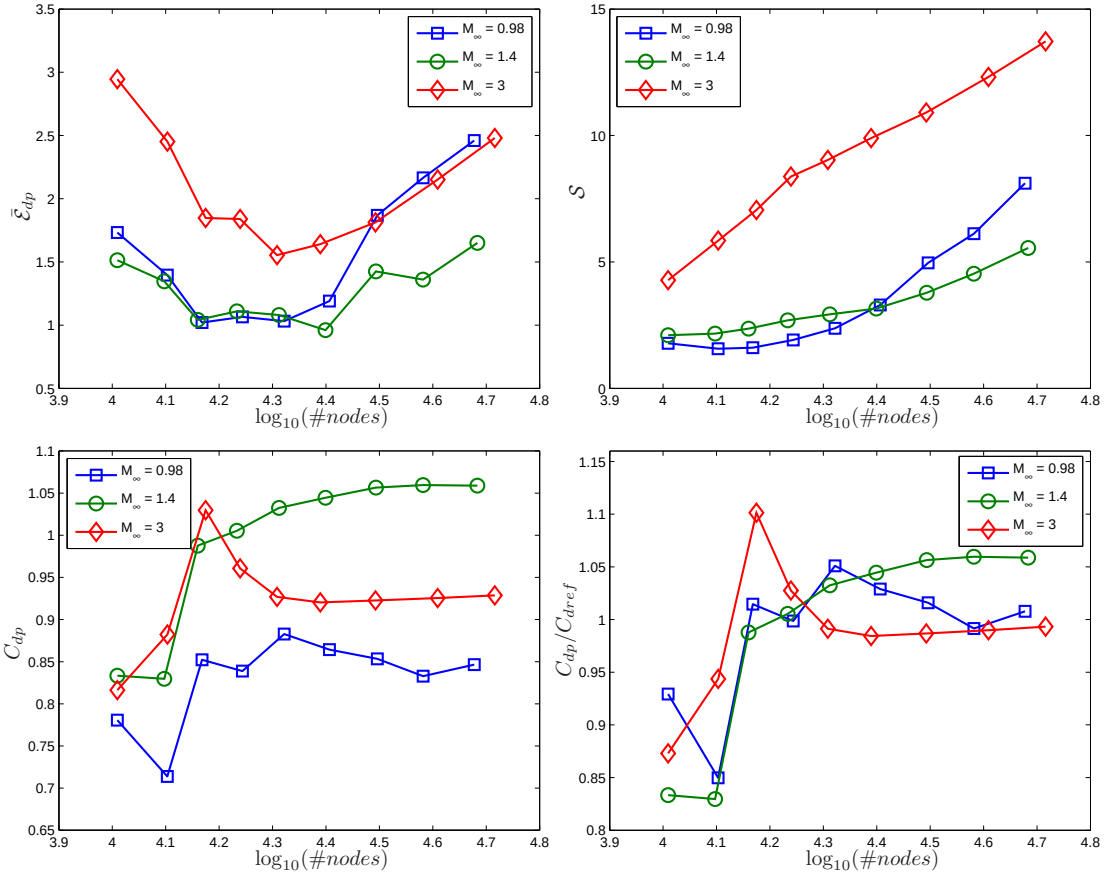

Figure 4. Sphere: log 10 of number of nodes or vertices versus the sum of error indicators $\bar{\mathcal{E}}_{dp}$, *(top-left)*, stability factor $\mathcal{S}$, *(top-right)*, drag coefficient C_{dp}, *(bottom-left)*, and the quality indicator C_{dp}/C_{dref}, *(bottom-right)*.

M_∞. The experimental observations show almost steady and symmetric patterns of the flow for $M_\infty > 0.9$. Therefore, we show one computation with $M_\infty = 0.8$, where we observe instability in the wake, and two computations with $M_\infty = 2, 3$ where the shock waves are dominant and the flow is almost steady. The corresponding reference values for drag are ~ 1.55, ~ 1.37 and ~ 1.25, respectively.

For the coarse meshes the instability of the turbulence wake in the transonic regime is absent. For $M_\infty = 0.8$ we solve the primal problem up to $t = 10$ and then solve the dual problem back in time to $t = 8$. The first plot of Figure 7 shows the drag coefficient for $M_\infty = 0.8$ from different adaptive iterations. We observe that at the final time the drag increases as the mesh is refined. The reason is that a turbulent wake develops for the fine meshes, but only after an initial start-up phase. We performed a larger computation just for the finest mesh until $t = 16$. The drag coefficient is plotted together with the experimental value at the top-right plot of Figure 7. The second row of the figure shows the drag for the supersonic regimes $M_\infty = 2$,

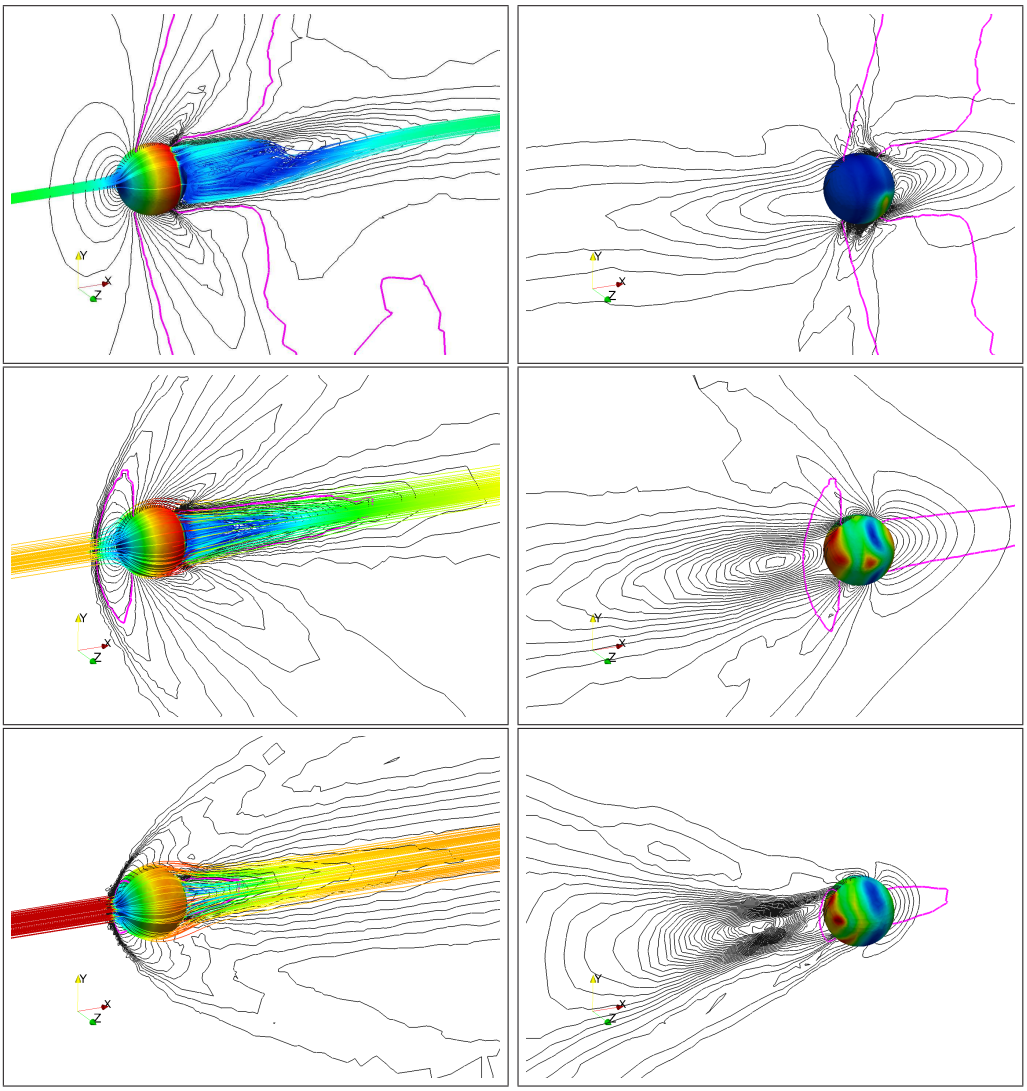

Figure 5. Sphere: Contours of the Mach number with the velocity streamlines at the left column; contours of the first component of the dual momentum at the right column. The first row: $M_\infty = 0.98$, contours: $0.0167267 \leq M \leq 2.14642$, $t = 10$, mesh: 57 442 vertices and 308 600 cells, *(left)*; contours: $-1.03707 \leq \phi_{m_1} \leq 7.60223$, $t = 8$, mesh: 57 442 vertices and 308 600 cells, *(right)*. The second row: $M_\infty = 1.4$, contours: $0.0114612 \leq M \leq 2.33017$, $t = 10$, mesh: 61 097 vertices and 329 604 cells, *(left)*; contours: $-0.798834 \leq \phi_{m_1} \leq 1.96303$, $t = 8$, mesh: 48 248 vertices and 261 525 cells, *(right)*. The third row: $M_\infty = 3$, contours: $0.00837154 \leq M \leq 5.34624$, $t = 10$, mesh: 66 546 vertices and 361 139 cells, *(left)*; contours: $-0.734578 \leq \phi_{m_1} \leq 4.10885$, $t = 8$, mesh: 52 003 vertices and 282 078 cells, *(right)*.

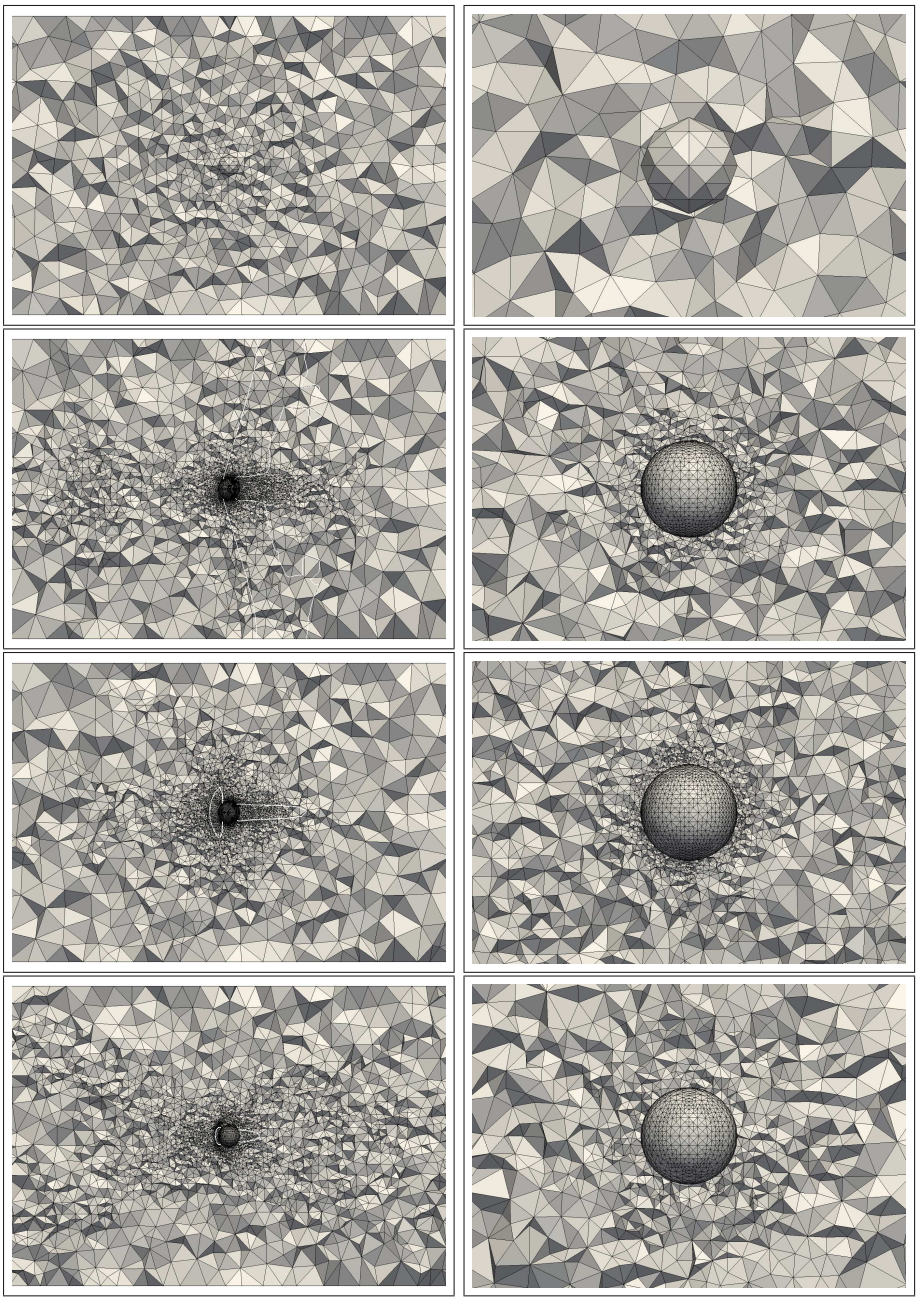

Figure 6. Sphere: meshes. The first row: initial mesh with 10 220 vertices and 55 492 cells; The second row: the final mesh for $M = 0.98$ with 57 442 vertices and 308 600 cells; The third row: the final mesh for $M = 1.4$ with 61 097 vertices and 329 604 cells; The fourth row: the final mesh for $M = 3$ with 66 546 vertices and 361 139 cells. The left column describes the xz-plane at $y = 0$ and the right column is a zoomed view of the sphere and the yz-plane at $x = 0.037$.

(left), and $M_\infty = 3$, (right). Figure 8 describes some computational details of the simulation: the number of nodes versus the total error indicators, the stability factor, the drag coefficients, and a quality indicator C_{dp}/C_{dref}. We observe that the computational values for the drag are slowly converging towards their experimental values. We observe that the stability factors increase slowly as function of number of nodes, whereas the error estimates decrease with mesh refinement.

Figure 9 shows the results of the computations from the last adaptive iteration. The left column of the figure describes the contours of the Mach number at the xy-plane at $z = 0.6$, together with the streamlines of the velocity close to the cylinder. The flow separates at the attached shock wave for all Mach numbers. The bow shock appears in the front of the cylinder for the supersonic cases. As we mentioned earlier, the flow is unstable for the transonic case $M_\infty = 0.8$, whereas it is almost steady for $M_\infty = 2$ and $M_\infty = 3$. The right column of the figure plots the contour of the first component of the dual solution ϕ_{m_1} at the xy-plane at $z = 0.6$, together with the sonic line. For the transonic case, the dual solution is unstable in the wake. The region where the sonic line attaches to the cylinder needs to be resolved for all Mach numbers. The dual solution indicates that the part of the bow shock orthogonal to the flow needs to be resolved for supersonic flows.

Figures 10 and 11 show the initial and adaptively refined meshes for each simulation. The figures are in the xy-plane at $z = 0.06$ and in the xz-plane at $y = 0$ respectively. After each iteration of the adaptive algorithm 5% of cells with the largest error contribution are marked for refinement.

6. Summary and conclusions

We have considered the problem of simulation turbulent compressible flow, where our focus is to develop a general method that is suitable for complex geometries, and which is robust and easy to implement. An adaptive finite element method has been presented, with high order stabilization in the form a residual based artificial viscosity, of the same general form as the shock capturing terms in e.g. SUPG, GLS and streamline diffusion methods. Contrary to these methods, for simplicity, we here drop the rest of the stabilizing terms, and we show that still the method is stable and can be used to approximate high Reynolds number compressible flow.

To use artificial viscosity as the only numerical stabilization in a finite element method has earlier been proposed in [18, 19], where a viscosity based on an entropy residual is used. The novelty in this paper is to instead use the standard residual.

What we propose is to use residual based stabilization as a unified method for numerical stabilization, shock capturing and turbulence capturing. The basic form of the shock-capturing stabilization reminds of the classical Smagorinsky subgrid model for LES, but with the rate of strain replaced by the residual, to assure consistency and high accuracy in smooth parts of the flow.

The adaptive algorithm is based on a posteriori error estimation with sensitivity information from the solution of a dual problem. This paper is an extension to compressible flow, of our previous work on adaptive turbulence simulation for incompressible flow [9, 10, 11, 15, 16].

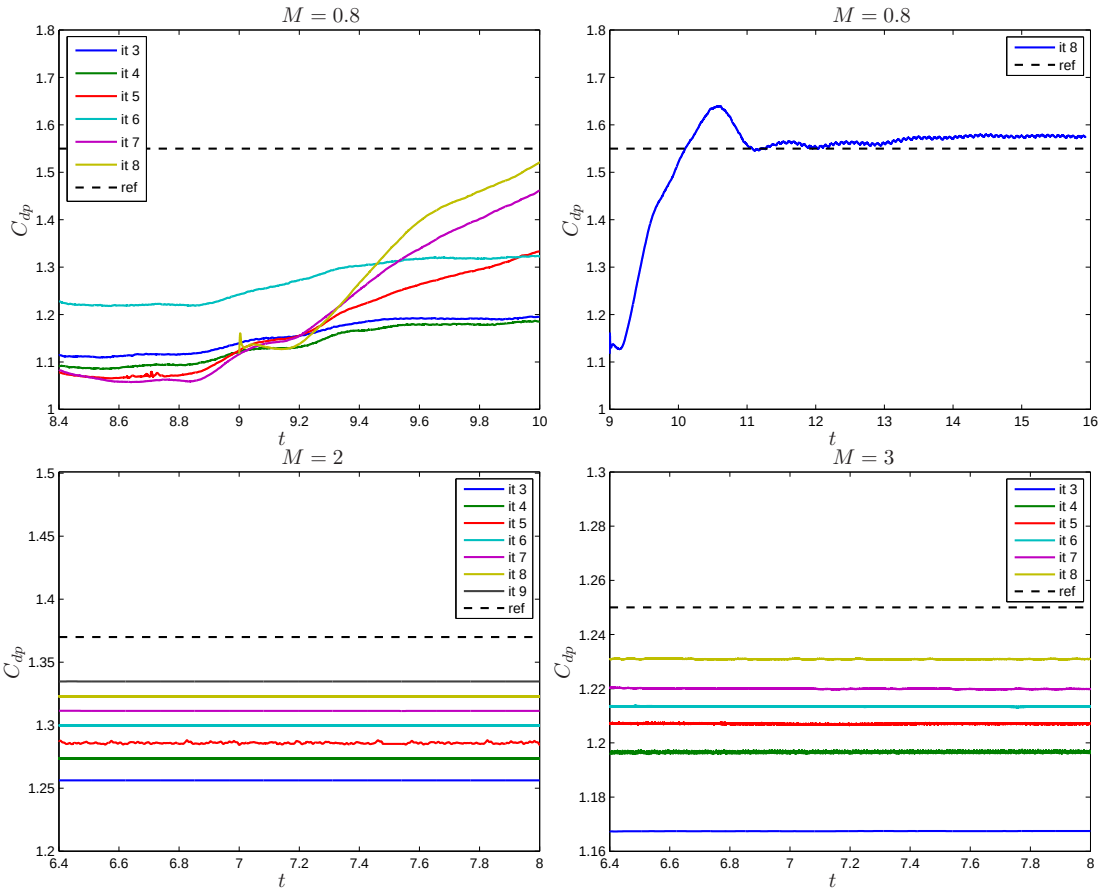

Figure 7. 3D cylinder: The drag coefficient C_{dp} versus time for different Mach numbers and adaptive iterations.

7. Acknowledgements

This work is supported by the European Research Council (ERC), the Swedish Research Council (VR), and the Swedish Foundation for Strategic Research (SSF).

REFERENCES

1. Nazarov M, Hoffman J. An adaptive finite element method for inviscid compressible flow. *International Journal for Numerical Methods in Fluids* 2010; **64**(188):1102–1128, doi:10.1002/fld.2335.
2. Sagaut P. *Large Eddy Simulation for Incompressible Flows*. Springer-Verlag, Berlin, Heidelberg, New York, 2001.
3. Woodward P, Colella P. The numerical simulation of two-dimensional fluid flow with strong shocks. *Journal of Computational Physics* 1984; **54**:115–173.
4. Richard Liska BW. Comparison of several difference schemes on 1d and 2d test problems for the euler equations. *SIAM, Journal of Scientific Computing* 2003; **25**:995–1017.

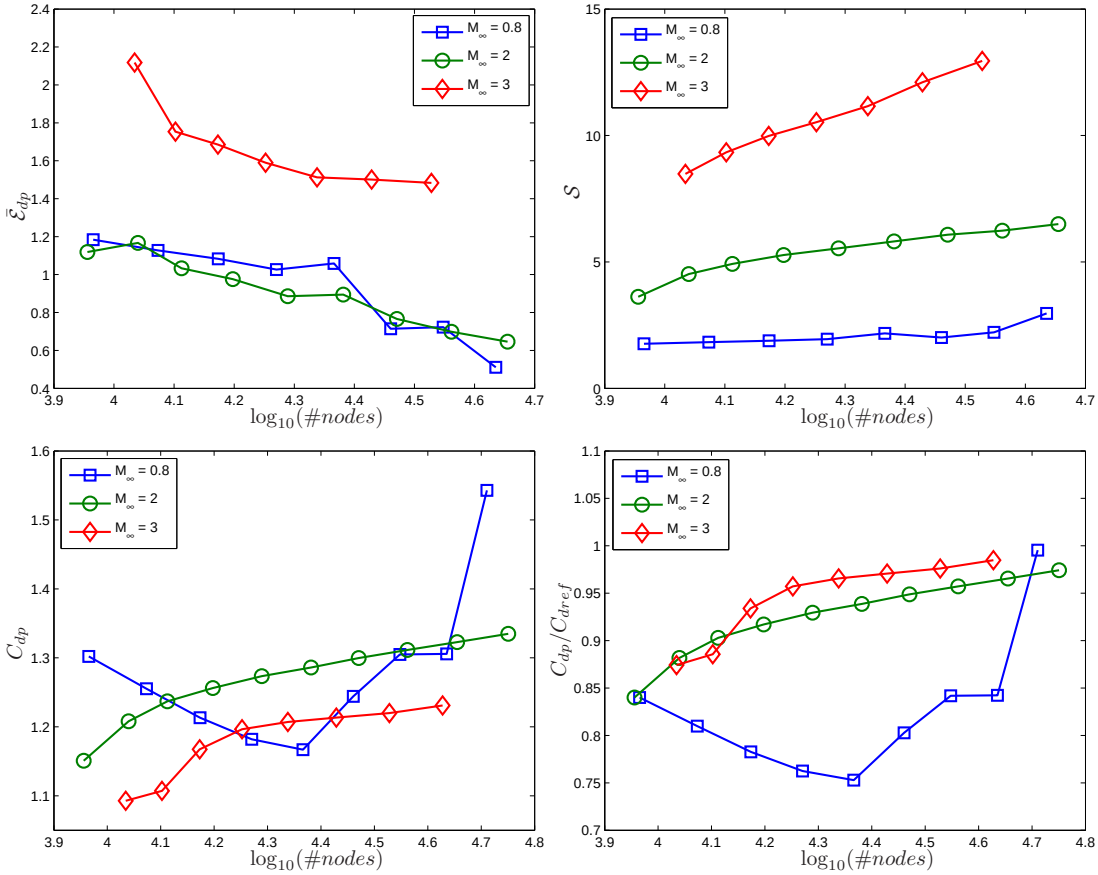

Figure 8. 3D cylinder: log 10 of number of nodes or vertices versus the sum of error indicators $\bar{\mathcal{E}}_{dp}$, *(top-left)*, stability factor $\mathcal{S}$, *(top-right)*, drag coefficient C_{dp}, *(bottom-left)*, and the quality indicator C_{dp}/C_{dref}, *(bottom-right)*.

5. Hughes TJR, Scovazzi G, Tezduyar TE. Stabilized methods for compressible flows. *SIAM, Journal of Scientific Computing* 2010; **43**:343–368, doi:DOI: 10.1007/s10915-008-9233-5.
6. Koobus B, Farhat C. A variational multiscale method for the large eddy simulation of compressible turbulent flows on unstructured meshes, application to vortex shedding. *Computer methods in applied mechanics and engineering* 2004; **193(15-16)**:1367–1383.
7. Farhat C, Rajasekharan A, Koobus B. A dynamic variational multiscale method for large eddy simulations on unstructured meshes. *Computer methods in applied mechanics and engineering* 2006; **195(13-16)**:1667–1691.
8. Cook AW, Cabot WH. Hyperviscosity for shock-turbulence interactions. *Journal of Computational Physics* 2005; **203(2)**:379–385.
9. Hoffman J, Johnson C. *Computational Turbulent Incompressible Flow: Applied Mathematics Body and Soul Vol 4*, Springer-Verlag Publishing, 2007.
10. Hoffman J, Johnson C. A new approach to computational turbulence modeling. *Computer Methods in Applied Mechanics and Engineering* 2006; **195**:2865–2880.
11. Hoffman J. Computation of mean drag for bluff body problems using adaptive DNS/LES. *SIAM, Journal of Scientific Computing* 2005; **27(1)**:184–207.
12. Fureby C, Grinstein FF. Monotonically integrated large eddy simulation of free shear flow. *AIAA Journal*

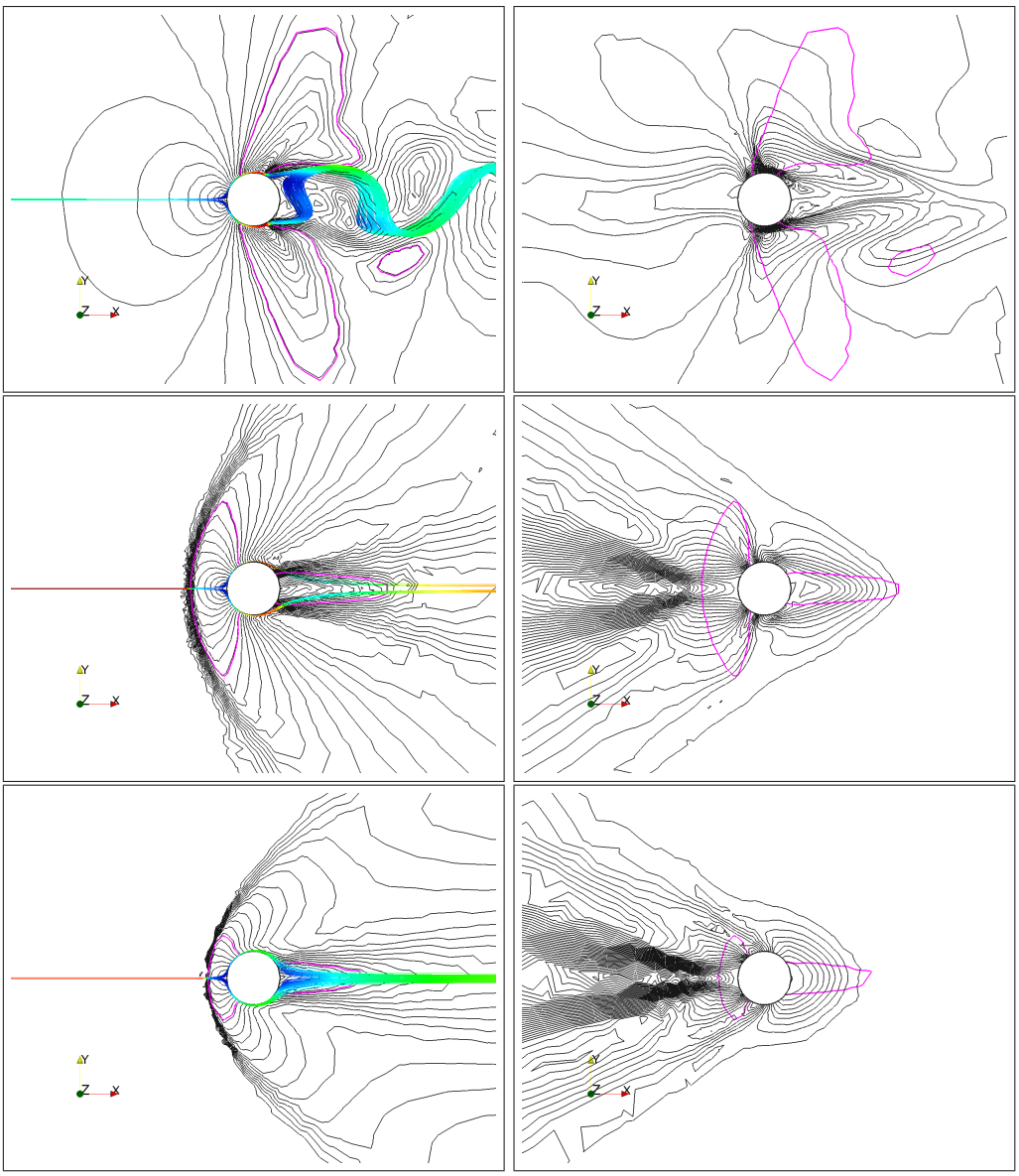

Figure 9. 3D Cylinder: Contours of the Mach number with the velocity streamlines at the left column; contours of the first component of the dual momentum at the right column, over the cut plane $z = 0.06$. The first row: $M_\infty = 0.8$, contours: $0.0165 \leq M \leq 1.92$, $t = 15.92$, mesh: 51 370 vertices and 265 344 cells, *(left)*; contours: $-2.516 \leq \phi_{m_1} \leq 3.8$, $t = 9$, mesh: the same as primal, *(right)*. The second row: $M_\infty = 2$, contours: $0.038 \leq M \leq 2.183$, $t = 8$, mesh: 56 304 vertices and 296 017 cells, *(left)*; contours: $-0.6 \leq \phi_{m_1} \leq 2.284$, $t = 6$, mesh: the same as primal, *(right)*. The third row: $M_\infty = 3$, contours: $0.028 \leq M \leq 3.2$, $t = 8$, mesh: 42 440 vertices and 220 216 cells, *(left)*; contours: $-0.916 \leq \phi_{m_1} \leq 2.7897$, $t = 6$, mesh: 33 742 vertices and 174 656 cells, *(right)*.

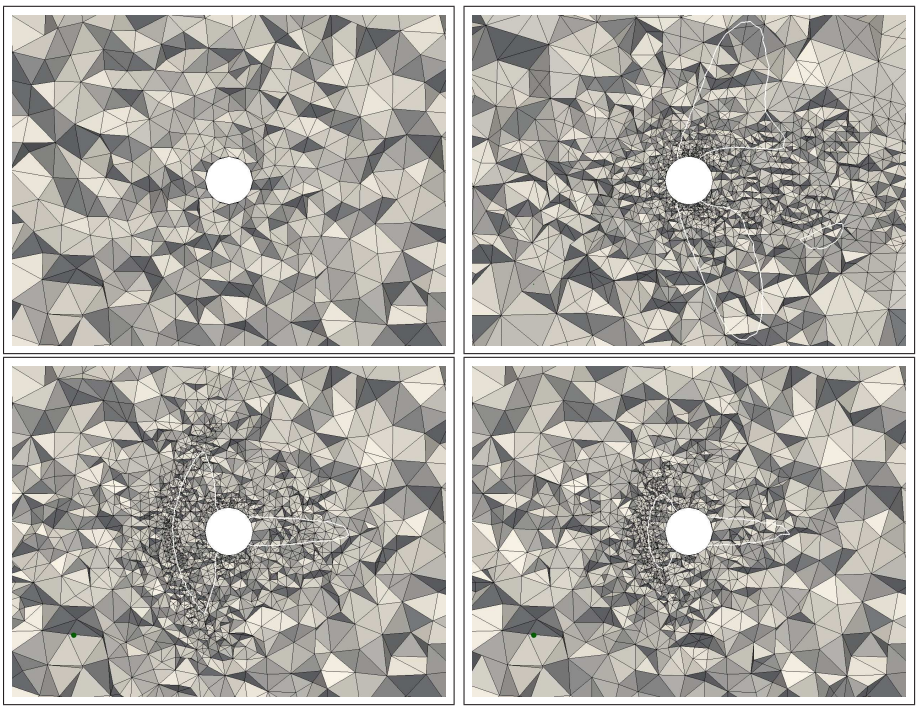

Figure 10. 3D cylinder: meshes. The first row: initial mesh with 9 034 vertices and 43 323 cells, *(left)*, the final mesh for $M = 0.8$ with 51 370 vertices and 265 344 cells, *(right)*. The second row: the final mesh for $M = 2$ with 56 304 vertices and 296 017 cells, *(left)*, the final mesh for $M = 3$ with 33 742 vertices and 174 656 cells, *(right)*. The figures are the xy-plane at $z = 0.06$, and the sonic line is plotted in white.

1999; **37(5)**:544–556.
13. Bazilevs Y, Calo V, Cottrell J, Hughes T, Reali A, Scovazzi G. Variational multiscale residual-based turbulence modeling for large eddy simulation of incompressible flows. *Computer methods in applied mechanics and engineering* 2007; **197(1-4)**:173–201.
14. Guasch O, Codina R. A heuristic argument for the sole use of numerical stabilization with no physical LES modeling in the simulation of incompressible turbulent flows. *Preprint Universitat Politecnica de Catalunya* 2007; .
15. Hoffman J. Adaptive simulation of the turbulent flow past a sphere. *Journal of Fluid Mechanics* 2006; **568**:77–88.
16. Hoffman J. Efficient computation of mean drag for the subcritical flow past a circular cylinder using General Galerkin G2. *International Journal of Numerical Methods in Fluids* 2009; **59(11)**:1241–1258.
17. Smagorinsky J. General circulation experiments with the primitive equations, part i: The basic experiment. *Monthly Weather Review, AMS Journals* 1963; **91**:99.
18. Guermond JL, Pasquetti R. Entropy-based nonlinear viscosity for fourier approximations of conservation laws. *Comptes Rendus de l'Acadéie des Sciences* 2008; **Ser. I, 346**:801–806.
19. Guermond JL, Pasquetti R, Popov B. Entropy viscosity method for nonlinear conservation laws. *Journal of Computational Physics* 2011; **230(2011)**:4248–4267.
20. Johnson C, Szepessy A. *Shock-capturing streamline diffusion finite element methods for nonlinear conservation laws*. Recent Developments in Computatioonal Fluid Dynamics, edited by T. J. R. Hughes and T. Tezduyar, AMD-Vol 95, 1988.
21. Rispoli F, Saavedra R, Menichini F, Tezduyar TE. Computation of inviscid supersonic flows around cylinders and spheres with the $\mathrm{V}-\mathrm{SGS}$ stabilization and YZβ shock-capturing. *Journal of Applied Mechanics* 2009; **76**(2):021209.

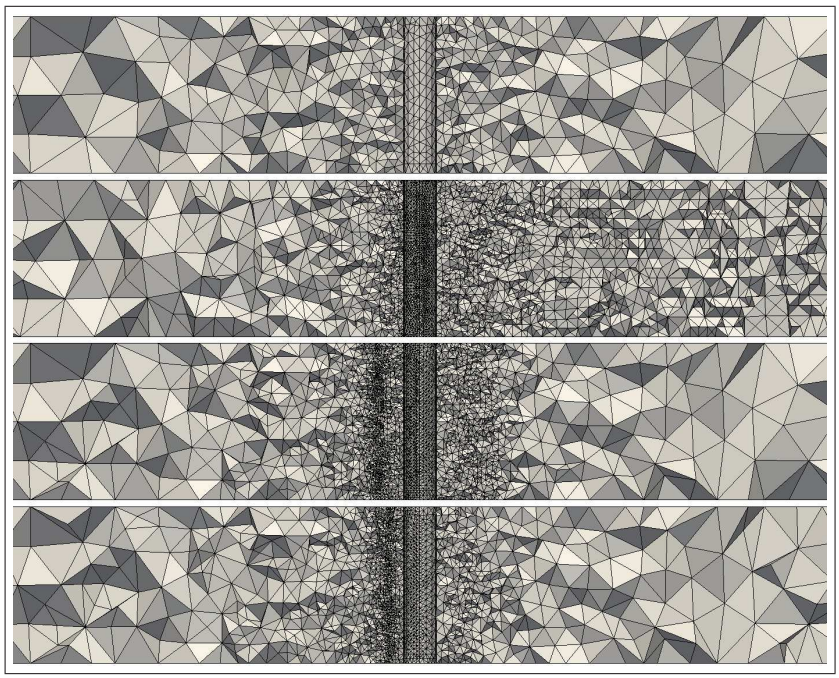

Figure 11. 3D cylinder: meshes. The first row: initial mesh with 9 034 vertices and 43 323 cells; The second row: the final mesh for $M = 0.8$ with 51 370 vertices and 265 344 cells; The third row: the final mesh for $M = 2$ with 56 304 vertices and 296 017 cells; The fourth row: the final mesh for $M = 3$ with 33 742 vertices and 174 656 cells. The plots describe the xz-plane at $y = 0$.

22. Cook AW, Cabot WH. A high-wavenumber viscosity for high-resolution numerical methods. *Journal of Computational Physics* 2004; **195(2)**:594–601.
23. Guermond JL, Prudhomme S. Mathematical analysis of a spectral hyperviscosity les model for the simulation of turbulent flows. *ESAIM: Mathematical Modelling and Numerical Analysis* 2003; **26**:893–908.
24. Guermond JL. On the use of the notion of suitable weak solutions in CFD. *International Journal for Numerical Methods in Fluids* 2008; **57**(9):1153–1170, doi:10.1002/fld.1853.
25. Vilela De Abreu R, Jansson N, Hoffman J. Adaptive computation of aeroacoustic sources for rudimentary landing gear. *proceedings for Workshop on Benchmark problems for Airframe Noise Computations I, Stockholm*, 2010.
26. Hughes T, Tezduyar T. Finite element methods for first-order hyperbolic systems with particular emphasis on the compressible euler equations. *Computer Methods in Applied Mechanics and Engineering* 1984; **45**(1-3):217–284, doi:DOI: 10.1016/0045-7825(84)90157-9.
27. Hughes TJR, Franca L, Mallet M. A new finite element formulation for computational fluid dynamics 1: Symmetrucal forms of the compressible euler and navier-stokes equations and the second law of thermodynamics. *Computer Methods in Applied Mechanics and Engineering* 1986; **54**:223–234.
28. Tezduyar T, Senga M. Stabilization and shock-capturing parameters in SUPG formulation of compressible flows. *Computer Methods in Applied Mechanics and Engineering* 2006; **195**:1621–1632.
29. Catabriga L, de Souza DAF, Coutinho ALGA, Tezduyar TE. Three-dimensional edge-based SUPG computation of inviscid compressible flows with YZβ shock-capturing. *Journal of Applied Mechanics* 2009; **76**(2):021208.
30. Guermond JL. Stabilization of Galerkin approximations of transport equations by subgrid modeling. *M2AN* 1999; **33(6)**:1293–1316.
31. Hughes TJR, Mazzei L, Jansen KE. Large eddy simulation and the variational multiscale method. *Computer methods in applied mechanics and engineering* 2000; **3**:47–59.

32. Szepessy A. Convergence of a shock-capturing streamline diffusion finite element method for a scalar conservation law in two space dimensions. *Mathematics of Computation* 1989; **53**:527–545.
33. Johnson C, Szepessy A, Hansbo P. On the convergence of shock-capturing streamline diffusion finite element methods for hyperbolic conservation laws. *Mathematics of Computation* 1990; **54(189)**:107–129.
34. Szepessy A. Convergence of a streamline diffusion finite element method for scalar conservation laws with boundary conditions. *Mathematical Modelling and Numerical Analysis* 1991; **25**:749–782.
35. Hughes T, Mallet M. A new finite element formulation for computational fluid dynamics. IV: A discontinuity-capturing operator for multidimensional advective-diffusive systems. *Computer methods in applied mechanics and engineering* 1986; **58**:329–336.
36. Löhner R. *Applied CFD techniques: an introduction based on finite element methods* (2nd edn). John Wiley & Sons, New York, 2008.
37. Nazarov M. Adaptive algorithms and high order stabilization for finite element computation of turbulent compressible flow. PhD Thesis, KTH, Numerical Analysis, NA 2011. QC 20110627.
38. Hoffman J, Johnson C. Blow up of incompressible euler equations. *BIT Numerical Mathematics* 2008; **48**:285–307.
39. Hartmann R, Houston P. Error estimation and adaptive mesh refinement for aerodynamic flows. *VKI LS 2010-01: 36th CFD/ADIGMA course on hp-adaptive and hp-multigrid methods, Oct. 26-30, 2009*, Deconinck H (ed.). Von Karman Institute for Fluid Dynamics, Rhode Saint Genèse, Belgium, 2009.
40. Hoffman J. On duality based a posteriori error estimation in various norms and linear functionals for LES. *SIAM J. Sci. Comput.* 2004; **26(1)**:178–195.
41. Hirsch C. *Numerical Computation of Internal and External Flows: Computational methods for inviscid and viscous flows, vol. 2,*. John Wiley & Sons, Chichester, 1990.
42. Murthy VS, Rose WC. Detailed measurements on a circular cylinder in cross flow. *A Journal* 1978; **16 no. 6**:549–550.
43. Chang CC, Lei SY. On the sources of aerodynamic forces: Steady flow around a cylinder or a sphere. *Proceedings: Mathematical, Physical and Engineering Sciences* 1996; **452**(1954):pp. 2369–2395.
44. Anderson JD, Anderson J. *Modern Compressible Flow: With Historical Perspective*. 3 edn., McGraw-Hill Science/Engineering/Math, 2002.
45. Miller DG, Bailey AB. Sphere drag at Mach numbers from $0 \cdot 3$ to 20 at Reynolds numbers approaching 10^7. *Journal of Fluid Mechanics Digital Archive* 1979; **93**(03):449–464.
46. Bailey A, Hiatt J. Free-flight measurements of sphere drag at subsonic, transonic, supersonic, and hypersonic speeds for continuum, transition, and near free molecular flow conditions. *Arnold Engng Development Ctr., Arnold Air Force Station, TN, Rep. AEDC-TR-70-291* 1971; .
47. Charters A, Thomas R. The aerodynamic performance of small spheres from subsonic to high supersonic velocities. *Journal of the Aeronautical sciences* 1945; **12**:468–476.
48. Walter L, Lange A. *Surface temperature and pressure distributions on a circular cylinder in supersonic cross-flow*. NAVORD Rep. 2854, 1953.